Chapter 6

In Situ Neutron Techniques for Studying Lithium Ion Batteries

Howard Wang,[1,2,5,*] R. Gregory Downing,[2] Joseph A. Dura,[3] and Daniel S. Hussey[4]

[1]Institute for Material Research and Department of Mechanical Engineering, State University of New York, Binghamton, NY 13902
[2]Material Measurement Laboratory, National Institute of Standards and Technology, Gaithersburg, MD 20899
[3]NIST Center for Neutron Research, National Institute of Standards and Technology, Gaithersburg, MD 20899
[4]Physical Measurement Laboratory, National Institute of Standards and Technology, Gaithersburg, MD 20899
[5]Department of Materials Science and Engineering, University of Maryland, College Park, MD 20742
[*]email: wangh@binghamton.edu

We review *in situ* neutron techniques for studying lithium ion batteries. Four neutron measurement techniques, neutron depth profiling, neutron reflectivity, small angle neutron scattering, and neutron imaging are discussed in this chapter. They are used to quantify the real-time distribution and transport of Li in active battery components during battery operation, and gain new insights in the function and failure of battery systems. We demonstrate that *in situ* neutron diagnoses offer new opportunities in better understanding the performance and lifetime of secondary batteries.

Introduction

Efficient energy storage will be an integral part of future energy solutions, in which alternative energy sources such as solar and wind will be extensively used, transportation with hybrid cars or all-electric vehicles will be the everyday norm, and portable devices and standalone electronics will be ubiquitous. Rechargeable

In Polymers for Energy Storage and Delivery: Polyelectrolytes for Batteries and Fuel Cells; Page, K., et al.; ACS Symposium Series; American Chemical Society: Washington, DC, 2012.

Li-ion batteries (LIBs) are a promising technology for efficient energy storage owing to the potential for high energy capacity, long cycle life, and low cost. Since the initial proposal by Whittingham in the 1970s (*1*), Li-ion batteries have evolved over three decades and have been commonly used in portable electronics such as laptop computers and mobile phones. However, to meet the high demands in large-scale energy storage needs such as plug-in hybrid electric vehicles (PHEV), renewable energy management, and power grid applications, battery technologies need to overcome many daunting challenges in order to significantly increase the energy and power capacities as well as safety and lifetime (*2–4*). Because of the transient and non-equilibrium nature of the materials and processes in a working LIB, much of the critical structural information is not easily accessible, greatly impeding the advances in the field. Precise, *in situ* diagnostic techniques will play a critical role in materials and process innovation, system optimization, safety analysis, failure diagnosis, and lifetime prediction in developing next generation LIBs.

Researchers have applied microscopy, spectroscopy, x-ray tomography, and scattering techniques to better understand the structure and performance of LIB systems. Particularly, insights are now gleaned from innovative use of *in situ* transmission electron microscopy (*5*, *6*), scanning probe microscopy (*7*, *8*), nuclear magnetic resonance spectroscopy (*9*, *10*), and synchrotron x-ray diffraction (*11*, *12*). Applications of neutron techniques for *in situ* diagnosis of LIBs are relatively new; however, they can be very powerful because of neutron's high penetration power and its relatively high sensitivity to lithium isotopes. Recently, *in situ* neutron diffraction has been successfully used to reveal changes in the crystal structures of electrode materials during battery operation (*13–20*).

There are many neutron measurement methods that are less frequently used by the battery research community. In this Chapter, four *in situ* neutron techniques are discussed: neutron depth profiling (NDP), neutron reflectivity (NR), small angle neutron scattering (SANS), and neutron imaging (NI). In addition to introducing fundamentals and physical principles of each technique, their potential applications to studying battery systems are illustrated with specific examples. Together they provide multi-scale measurements of the Li distribution and transport in active LIBs to yield valuable new insights in the performance and failure of battery systems.

Neutron Depth Profiling

As most LIBs operate with the so called rocking chair mechanism, in which Li ions are shuttled back and forth between cathode and anode layers, it is of great interest to directly visualize the distribution of the mobile ingredient, Li, in a LIB during its operation. Simultaneous space- and time-resolved Li measurements allow for direct comparison of ionic motion in the battery with the electric current in the external circuit, which would provide irreplaceable insights in addressing issues related to transport mechanisms, structure integrity, normalcy of performance, and reliability of operation. Based on the neutron activation and the energy loss spectrum of energetic ions in matter, NDP has been applied to

In Polymers for Energy Storage and Delivery: Polyelectrolytes for Batteries and Fuel Cells; Page, K., et al.;
ACS Symposium Series; American Chemical Society: Washington, DC, 2012.

resolving nano- to micro-scale lithium distributions in working battery systems during charge/discharge cycles.

NDP is an analytical technique for quantitative measurements of a list of technologically important elements (Li, B, N, He, Na, etc) as a function of depth into a solid surface (*21*). Initially developed in the early 1970's for measuring boron distributions in silicon wafers (*22*), and until recently applied mostly to studying electronics materials, NDP is now a mature technique, increasingly used to measure lithium distributions in modern battery technologies (*23–28*).

The NDP setup is schematically illustrated in Figure 1. This arrangement is typical of the instrument operated at the National Institute of Standards and Technology (NIST) (*21*). In an NDP measurement, a flux of cold neutrons coming out of a neutron guide pass through a Li-containing specimen and react with the isotope ^{6}Li to generate two highly energetic charged particles, $^{6}Li + n \rightarrow \alpha + {}^{3}H$. Both the charged particle energy spectrum and the total neutron fluence that passes through each sample are monitored and recorded with surface barrier detectors. The majority of neutrons that enter the chamber pass through the sample, exit the sample chamber, and are absorbed by the beam stop. Because the incoming energy of the neutron is negligible (< 4 meV) and the interaction rate is small, typically < 0.01% of the incoming fluence, NDP is considered a non-destructive technique, an obvious advantage in battery studies.

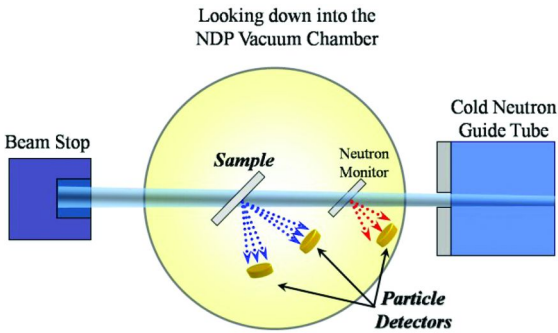

Figure 1. Schematic illustration of NDP setup.

The tritium and the recoil α particles emitted from the reaction each have a well-known energy determined by the reaction kinematics (2727 keV and 2054 keV respectively). The total number of charged particles emitted from the sample is proportional to the product of the neutron fluence that impinges upon the sample, the reaction cross-section of the nuclides (*ca.* 2089 barns for ^{6}Li and 4 meV neutrons), and the nuclidic abundance throughout the illuminated volume. Using cold neutrons enhances the reaction cross-section and enables measurement at higher rates or better statistics. The charged particles travel diametrically away from the reaction center, and lose energy to the matrix at a rate (the stopping power) that depends on the energy of ions and the electronic structures of the matrix (*21*). The energy of the detected particles is used to determine the initial location of the activation reaction; the normalized counts are used to measure the abundance of elements at the corresponding depth.

In Polymers for Energy Storage and Delivery: Polyelectrolytes for Batteries and Fuel Cells; Page, K., et al.;
ACS Symposium Series; American Chemical Society: Washington, DC, 2012.

NDP has similarities to ion beam techniques, such as forward recoil spectrometry (FRES) and Rutherford backscattering spectrometry (RBS), it enables the measurement of depth profiles of flat solid specimens over an area of *ca.* 1 mm^2 to $>10^2$ mm^2, conveniently defined by the aperture of a mask covering the sample. The full depth range of the profile varies from a few micrometers to 10s of micrometers, depending on the atomic composition of the specimen as well as the particle of detection, α or ^3H. Likewise, the depth resolution varies from a few nanometers to a few hundred nanometers. There are also important differences in the abovementioned techniques that make them complimentary. RBS is most useful for determining heavy elements in low atomic number matrix materials. As both FRES and NDP are good for profiling light elements, FRES requires the use of an energetic (MeV) ion beam of heavier elements to knock out the light elements for measurements, whereas NDP uses an meV neutron beam which causes little energy deposition, avoiding heating and damaging the specimen. Another consequence of the nuclear activation *vs.* ion beam is that NDP has superior energy resolution to those techniques because the well-defined kinetic energies of detecting particles at the reaction. In addition, the selective nature of nuclear activation ensures that Li spectra are clean, being free of interference from other elements. These differences represent a significant advantage of NDP for continuous *in situ* measurement of Li transport during prolonged battery operation.

The distribution of Li in working batteries undergoing charge/discharge cycles has been measured using *in situ* NDP at NIST. One example of *in situ* NDP real-time assessment on the battery operation is shown in Figure 2. The battery was fabricated by sputter deposition of thin films, with a layered structure of mica / Pt (200 nm) / $LiCoO_2$ (5 μm) / LiPON (2 μm) / Li (4 μm) / Pt (200 nm) / mica, where $LiCoO_2$ is the cathode and Li metal is the anode. The mica encapsulating window has to be thinned down to *ca.* 15 μm in order for the $^3H^+$ to escape the packaging layers and reach the detector. NDP spectra recorded during the charge/discharge are shown in Figures 2(a) and 2(b), respectively. Each spectrum was collected during a period of 15 min and consecutive spectra are 75 min apart (one of every five spectra plotted for clarity). The Li metal layer is shown as a prominent peak around 1200 keV, while the $LiCoO_2$ layer is shown as the plateau about 1700 keV to 2100 keV. In the charge cycle, Li is pumped out from the $LiCoO_2$ cathode layer and deposited in the anode, while in discharge, Li flows back from the anode to cathode.

Figure 3(a) shows the potential profiles of the battery during several cycles of charge/discharge. Using SRIM software to calculate the stopping power of $^3H^+$ in different battery layers (*29*), NDP data are quantitatively analyzed to yield lithium depth profiles, allowing for direct comparison of Li transport inside the battery and the electric current flow in the external circuit. Figure 3(b) compares the Li ion density in the cathode measured by NDP (symbols) and displaced electric charge recorded by the potentiostat (lines). (Note: throughout this chapter error bars represent a one sigma standard deviation.) A good match is maintained till the instability occurs as indicated by the erratic responses of current and potential during the second discharge, which may relate to sudden structural changes in the battery. The discrepancy between the ionic transport in the cathode and the electric

In Polymers for Energy Storage and Delivery: Polyelectrolytes for Batteries and Fuel Cells; Page, K., et al.;
ACS Symposium Series; American Chemical Society: Washington, DC, 2012.

transport in the external circuit could be a powerful indicator of the onset of battery failure, which is illustrated here using time-resolved NDP.

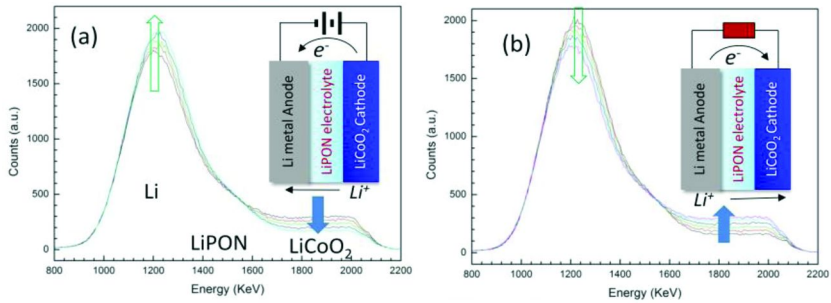

Figure 2. Time-resolved in situ NDP on a thin film battery during (a) charging and (b) discharging. The assignment of electrode ane electrolyte layers in the spectra are labeled. Arrows indicate the flow of Li in each electrode.

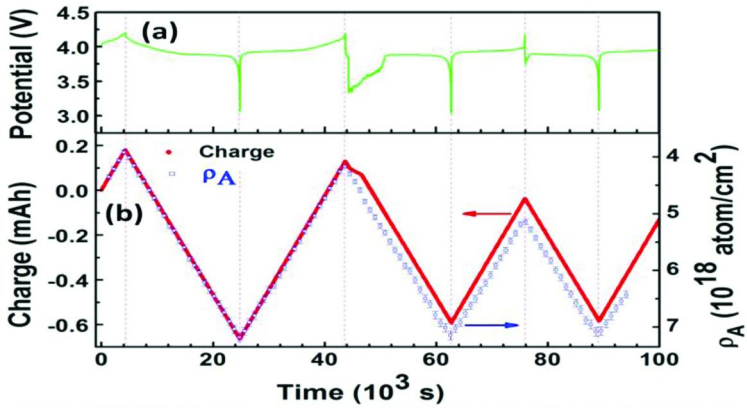

Figure 3. Time-resolved (a) potential profile, and (b) electric vs. ionic charge displacement. The potential anomaly at the beginning of the second discharge coincides with the mismatched charge at the same time.

Although thin film solid state batteries are used here to illustrate the utility of *in situ* NDP, the technique can be readily applied to any Li-containing batteries prepared in layered structures and operatable in vacuume. With higher neutron flux and better detection capability, NDP could be further improved to become a powerful tool to probe the reliability and lifetime of Li-containing batteries under real operation circumstances. Fast NDP measurement will be particularly useful for understanding battery performance at high charge/discharge rates, which is critical for vehicle applications.

In Polymers for Energy Storage and Delivery: Polyelectrolytes for Batteries and Fuel Cells; Page, K., et al.; ACS Symposium Series; American Chemical Society: Washington, DC, 2012.

Neutron Reflectivity

Most lithiation and delithiation processes involve compositional and structural changes in electrode materials, most notably volume expansion and retraction. Precise measurements are needed in order to quantify these variations at sub-nanometer levels particularly near interfaces. As the bulk of a crystalline structure expands, a lattice parameter change or phase transition can be measured with diffraction techniques, which, however, do not readily quantify amorphous materials. Furthermore, the composition and structure across interfaces between different components in batteries are of critical importance to the transport of Li ions and electrons. Precisely measuring these structures to sub-nanometer scales is critical to understanding interfacial phenomena.

One prominent example is the structure and composition of the solid electrolyte interface (SEI) layer that forms on electrodes from the breakdown of the electrolyte, which is crucial for the reliable operation of batteries. Recent NR measurements are the first of their kind in determining the thickness of the SEI as a function of potentiostatic voltage (*30*). The sensitivity of NR for light elements and for different isotopes of certain elements including H and Li makes it ideally suited for Li battery research. Furthermore, since single crystals such as Si are relatively transparent to the neutron beam, NR can be applied to *in situ* characterization of electrode films and their interfaces deposited onto a flat Si substrate and enclosed in wet chemical cells, similar to those developed for studying hybrid lipid bilayer membranes (*31*), except that a fully enclosed cell is often used in battery studies to avoid the corrosion of the substrate and the contamination of electrolytes.

NR is a high resolution technique for probing structure, composition and magnetism in thin films with sub-angstrom accuracy for films as thin as 1.5 nm (*32*, *33*). It is commonly used to measure liquid/gas interfaces (*34*), and biological (*35*, *36*), hydrogen related (*37*, *38*) polymer (*39*), water containing materials such as polymer electrolyte membranes (*40*), and magnetic thin films (*41*), or combinations of these phenomena (*42*). Typically thin films are characterized using specular neutron reflectometry (*43*, *44*), in which a monochromatic neutron beam of wavelength λ is directed onto thin layers on a flat substrate at a glancing angle, θ. The intensity of the reflected beam at the same angle relative to the sample [Figure 4(a)] is recorded as a function of the amplitude of momentum transfer vector normal to the film surface, Q_z, defined as: $Q_z=(4\pi / \lambda) \sin\theta$. NR data are used to determine the scattering length density (SLD) as a function of depth or $\rho(z)$ defined (ignoring magnetic contributions) as: $\rho(z) = \Sigma_j N_j(z) b_j$, where $N_j(z)$ is the number density of isotope j at depth z, b_j is the coherent nuclear scattering length of isotope j. The atomic dependence through b_j allows the SLD profile to be interpreted as a compositional profile when the constituent materials are known. Furthermore, the isotopic dependence of b_j allows for specific components of a system to be labeled during sample preparation and followed as the sample evolves during an experiment.

Specular NR is not sensitive to in-plane structures and interacts with the SLD which is averaged in the plane of the sample over any compositional variations within the neutron coherence length, as depicted by the dashed line in

In Polymers for Energy Storage and Delivery: Polyelectrolytes for Batteries and Fuel Cells; Page, K., et al.;
ACS Symposium Series; American Chemical Society: Washington, DC, 2012.

the two dimensional rendition of a multilayer structure shown in Figure 4(a). The corresponding SLD depth profile is shown in Figure 4(b). Neutrons reflected from each interface in multilayered thin films interfere constructively or destructively as a function of Q_z, resulting in oscillatory reflectivity, whose periodicities are inversely proportional to the thickness of the layers that have caused the interference. As large surface and interfacial roughnesses seriously deteriorate the quality of NR spectra, it is essential to prepare films with sub-nanometer roughness in order to take advantage of the high resolution technique.

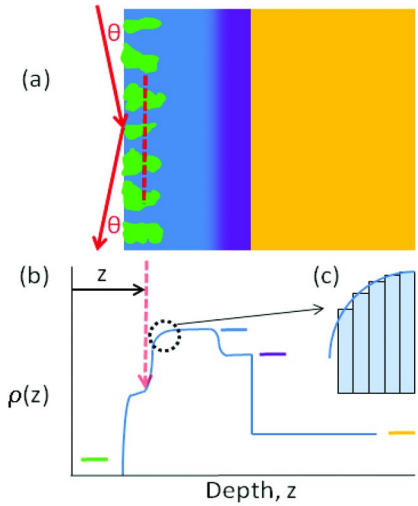

Figure 4. Schematics of NR measurement. (a) A cross section view of a multilayer structure, (b) the simulated SLD profile, and (c) details of the profile approximation.

Because NR measures the reflected intensity rather than the amplitude, the phase of the neutron wave is not measured; therefore, single NR spectra cannot be directly inverted to determine a SLD profile. Although approaches have been developed for direct inversion (*45*), the more widely used method of determining the depth profile is through model fitting. Simple structures can be modeled as single layers of constant SLD for each film. More complicated profiles, such as rough interfaces or compositional gradients, can be modeled as a stack of arbitrarily thin layers; this can be applied to approximate any SLD profile [Figure 4(c)]. In fitting, SLD profile models are created and iteratively adjusted through least square refinement until the simulated scattering plot matches the dataset. The software (*46*) used for this is based upon the Parratt formalism (*47*).

The battery assembly for *in situ* NR measurements is schematically illustrated in Figure 5(a). It consisted of a half cell of eleactron-beam evaporated Cu (5 nm) / a-Si (10 nm) / Al_2O_3 (2 nm) films on a Si substrate as the active electrode, Li metal as the counter and negative electrode, and 1 mol/L $LiPF_6$ in EC:DMC (1:1 by volume) solution as the electrolyte. The cell was sealed using a 0.7 mm thick viton gasket, and the electrodes were connected to a potentiostat through thin gold

In Polymers for Energy Storage and Delivery: Polyelectrolytes for Batteries and Fuel Cells; Page, K., et al.; ACS Symposium Series; American Chemical Society: Washington, DC, 2012.

leaves. NR data were taken after the initial assembly (noted as open circuit, or OC), and after the first and sixth lithiation and delithiation, as shown in Figure 5(b). The curves through symbols are the calculated reflectivity from the best fits. The fitting results in Figure 6(a) show that the Si film swells from the initial thickness of 11 nm to 16 nm upon first lithiation, and shrinks back to 12 nm upon delithiation. Similar behaviors are observed upon sixth lithiation and delithiation. Corresponding Li compositions appear to be consistent with the Si film swelling/ shrinking [Figure 6(b)]. The results indicate that increasing amounts of residual Li are left in the sample after delithiation as a function of the number of cycles. The integrity of both the a-Si and Al_2O_3 layer remains largely intact during the operation, presumably due to the shallowness of the lithiation/delithiation.

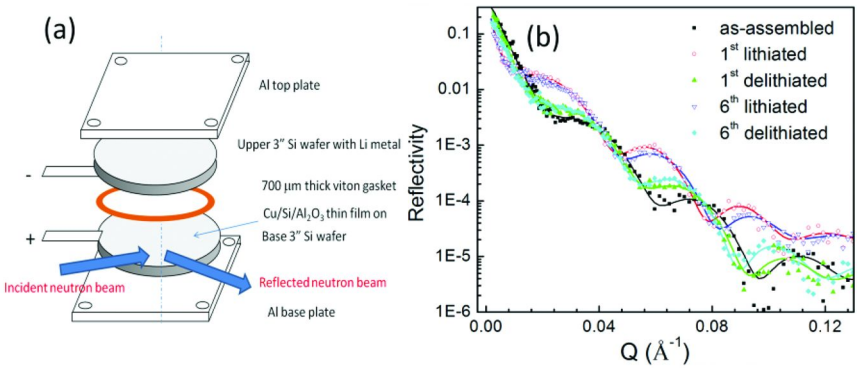

Figure 5. (a) schematics of battery assembly for in situ NR measurements, and (b) NR spectra at various charge states showing mostly reversible structural variations.

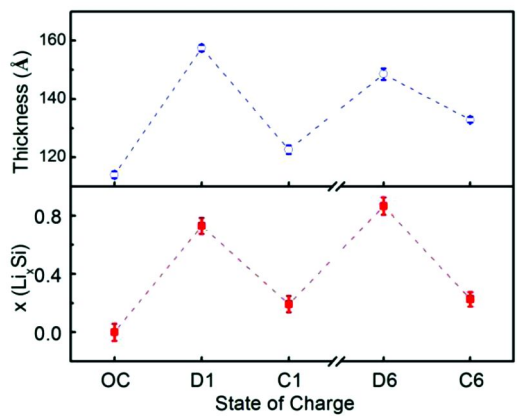

Figure 6. (a) The thickness of Si electrode, and (b) the Li composition at various charge states. The lines are a guide to the eye.

In Polymers for Energy Storage and Delivery: Polyelectrolytes for Batteries and Fuel Cells; Page, K., et al.; ACS Symposium Series; American Chemical Society: Washington, DC, 2012.

As demonstrated in this example, NR offers the unique capability of sub-nanometer resolution measurements of buried interfaces and films, which are much needed for advancing fundamental understanding of LIB materials and systems. Critical LIB issues to be addressed using NR include the mechanism of lithiation/delithiation of active materials, the formation of solid electrolyte interface, degradation and dissolution of electrodes, and the structure of electrolytes near solid surfaces.

Small Angle Neutron Scattering

Nanoscale morphology has become an increasingly important topic in battery research since much of the transport behavior and structural integrity issues rely on details near surfaces and at nanoscales. Nanoscale engineering is also considered a key element in addressing the issue of the low power density of batteries (*48*) as large surface areas and small diffusion lengths assure fast charge/discharge kinetics. To avoid compromising the system-level energy and powder density, nanoscale materials need to be densely packed into bulk composites when included as active components in batteries. The structure variation of such materials is best monitored using small angle neutron scattering, SANS. In particular, SANS measures two aspects, direct structure measurement such as swelling and recovery of nanoscale grain in a bulk assembly, and the contrast changes due to the lithiation-induced scattering length density variation.

In a SANS measurement, incident neutrons with a wavelength λ, typically in the range of 5 Å to 20 Å, impinge on the sample, and scattered neutrons are counted using a 2-dimensional (2D) area detector (see Figure 7). Several measurements including the direct beam intensity, background noise, sample transmission, empty cell scattering, and detector efficiency, are needed to correctly obtain the sample scattering. The absorption of neutrons by Li is small in a typical SANS battery cell, and is quantitatively accounted for by the sample transmission. For samples with assumed isotropic pore geometry, the corrected 2D intensity is circularly averaged to yield the total scattering cross section of the sample, which includes the incoherent scattering (*49*). The scattering intensity, I, is obtained as a function of momentum transfer vector, $Q=(4\pi / \lambda \sin\alpha/2)$, where α is the scattering angle. In a typical SANS experiment, several sample-to-detector distances from 1 m to 15 m can be used to obtain a wide Q-range (~0.001 $Å^{-1}$ to ~0.5 $Å^{-1}$) covering structural length scales from ~ 1 nm to ~ 200 nm. The neutron wavelength dispersion is mainly responsible for the resolution of the SANS measurements.

SANS has been widely used to measure nanoscale structures in bulk phases. Time-resolved *in situ* SANS, TR-SANS, has found relatively limited applications in battery research because of the small neutron fluence rate and low scattering. In recent years, the increase in flux at the reactor-based NIST instruments and deployment of the spallation neutron source at ORNL make it possible to study nanoscale phenomena in LIB in real time. In the following example, TR-SANS measurements were performed with the NG-7 30 m SANS instrument at the NIST Center for Neutron Research.

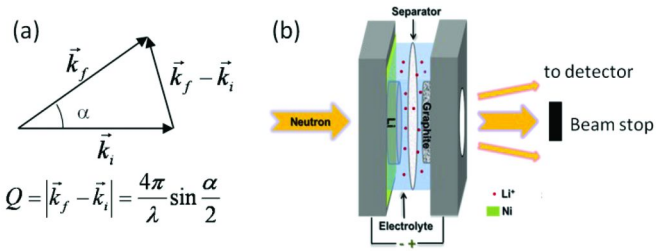

Figure 7. (a) Neutron momentum transfer in SANS; (b) schematics of a battery cell for SANS

The battery assembly consists of graphite composite *vs.* Li electrodes for studying lithiation and delithiation processes in the graphite electrode as schematically shown in Figure 7(b). A neutron beam passes through a stack of two 1 mm thick quartz plate windows, two 10 μm thick Ni foils as current collectors, 300 μm thick Li anode, 1 mol/L $LiPF_6$ in EC:DMC (1:1 by volume) solution as electrolyte, 25 μm thick polypropylene separator, and *ca.* 15 μm thick graphite composite electrode in the normal direction, with scattering occurring mostly from the graphite electrode, which is composed of platelet graphite particles of *ca.* 10 μm wide and 1-2 μm thick, carbon black, and polyvinylidene fluoride (PVDF). SANS spectra of the initial state (squares) and the fully lithiated state (triangles) are shown in Figure 8. The variation of the scattering intensity upon charge/discharge is small compared to the overall intensity. A dominant scattering feature in the Q-range is the ~Q^{-4} power law behavior, which is characteristic Porod scattering law due mostly to interfacial contributions.

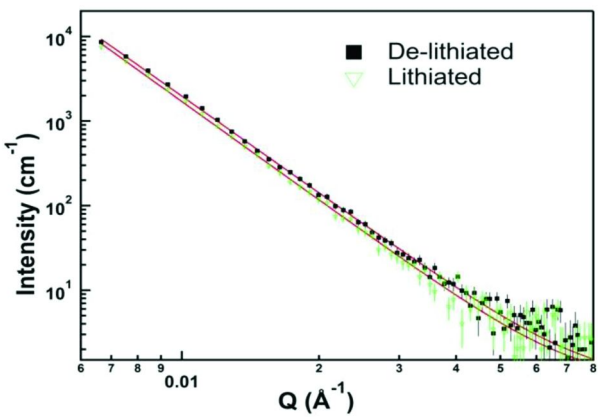

Figure 8. SANS spectra of delithiated (squares) and lithiated (down triangles) states.

In Polymers for Energy Storage and Delivery: Polyelectrolytes for Batteries and Fuel Cells; Page, K., et al.; ACS Symposium Series; American Chemical Society: Washington, DC, 2012.

The charge/discharge current [Figure 9(a)], potential [Figure 9(b)], and electric charge displacement [Figure 9(c)] profiles recorded during SANS measurements indicate the typical performance of a graphite anode. The variation of integrated SANS intensity upon cyclic charge/discharge is shown in Figure 9(d), which rises and falls in apparently full synchronization with charge states. This is due to the contrast variation induced by lithiation/delithiation. As Li intercalates into graphite particles, the overall SLD decreases, reducing the contrast with the matrix, hence decreasing the scattering intensity, and vice versa with de-intercalation. However, as the charge transfer becomes shallower at higher cycling rates, the amplitude of the intensity variation becomes even larger. This is contradictory to the prediction that the contrast variation is the only source of the scattering intensity change. The excess scattering could result from new surfaces created due to fracturing of graphite particles.

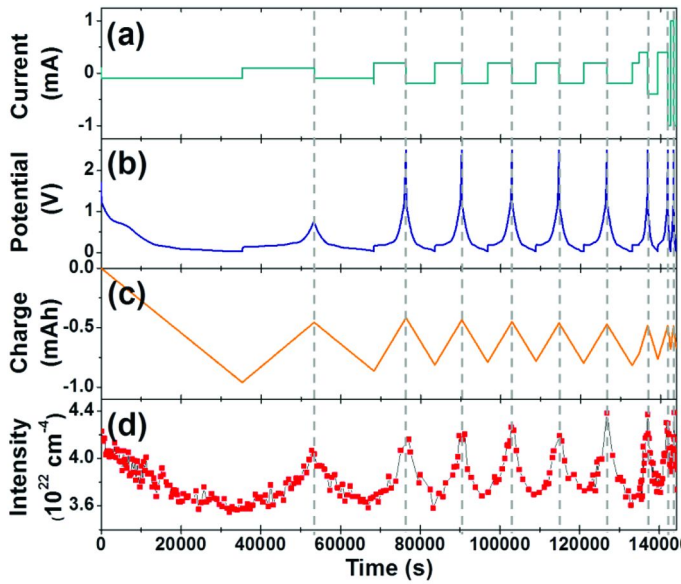

Figure 9. The evolution of (a) current, (b) potential, (c) charge displacement, and (d) integrated SANS intensity during charge/discharge cycles.

This observation is particularly interesting because fresh surfaces from the fracture will be immediately passivated by new SEI layers, which consume Li in the battery, resulting in the reduction of the reversible energy storage capacity. Lithiation-induced fracturing of graphite particles in the anode has been one cause of the irreversible capacity loss during LIB operation. Quantitative *in situ* monitoring of the generation of new surface areas will assist the development of materials and process recipes for improved cycle life. There are studies on this topic using *ex situ* Raman spectroscopy and electron microscopy (*50*). *In situ* diagnosis by scanning probe (*51*) acoustic emission measurement (*52*) has

In Polymers for Energy Storage and Delivery: Polyelectrolytes for Batteries and Fuel Cells; Page, K., et al.;
ACS Symposium Series; American Chemical Society: Washington, DC, 2012.

also been developed. Nevertheless, those techniques offer mostly indirect and qualitative measurements of fracture surfaces.

Although the case of graphite particle fracturing is discussed here, such approach can be applied to other electrode materials that are faceted and fracture brittlely. SANS can be a unique *in situ* technique for monitoring both the bulk and interfacial activities of individual grains in active components in batteries. In the example discussed above, hydrogenated electrolyte solvent was used; there is little contrast between the electrolyte and the SEI layer formed from the decomposition of the electrolyte molecules because of their similar overall isotopic compositions. However, by selective labeling of molecules in the electrolyte, SANS could be used to determine the reactivity of different species from the resultant interfacial scattering signals upon battery operation. Such capabilities for surface detection, together with its conventional strength for monitoring the size and shape of nanoscale structures in real time, *in situ* SANS could be a very powerful tool in understanding the operation of LIBs going through lithiation/delithiation cycles.

Neutron Imaging

The electrode of a practical LIB is a complex composite designed to facilitate ionic and electric transport while maintaining mechanical integrity. Non-uniform physical structures and processes, coupled with heterogeneous chemical activities at surfaces and in the bulk of battery materials result in the heterogeneity in electrochemical processes at both the electrode and individual grain levels. Much of the difficulty in accurate modeling of battery performance lies in the uncertainty of the ionic and electric transport pathways. That has led to recent efforts in the tomography of electrode materials (*53*). Visualization of non-uniformity is difficult, particularly in a real battery environment. Neutron imaging (or neutron radiography) offers the promise of direct visualization of hotspots and non-uniform fields of transport in lithiating electrodes.

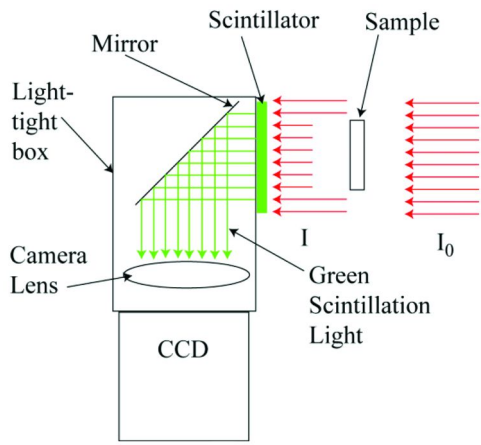

Figure 10. Schematic illustration of neutron imaging.

In Polymers for Energy Storage and Delivery: Polyelectrolytes for Batteries and Fuel Cells; Page, K., et al.;
ACS Symposium Series; American Chemical Society: Washington, DC, 2012.

Neutron radiography measures spatially the change in transmission of an object as a function of time compared to a reference state. A sketch of the sample area for neutron imaging is shown in Figure 10. Neutrons impinge on the sample from the right. The sample is mounted as close to the scintillator screen as possible and is exposed to ambient conditions. Neutrons are absorbed by Gadolinium in the gadoxysulfide scintillator, and the energetic conversion electrons result in the emission of green light. A camera lens attached to the charge-coupled device (CCD) collects and focuses light onto the sensor and enables tailoring the field of view and spatial resolution to the sample under study by varying the focal length. A mirror at 45° enables locating the radiation sensitive CCD camera out of the direct beam path of unabsorbed neutrons and gamma rays emanating from the reactor core. The scintillator, mirror, lens and camera are housed in a light-tight box to reduce the background. Neutron images are continuously recorded.

Neutron radiography is attractive for battery research due to the direct measurement of the change in Li concentration. There are applications of NI to battery studies (*54–57*), which take advantage of the high penetrating power of neutrons and the high contrast with Li containing materials, particularly with ^{6}Li isotope because of its large activation cross-section. It is possible to image at high spatial resolution or high time resolution, with a trade-off required to obtain a given uncertainty in the areal number density (*58*). At high spatial resolution (~10 μm), it is possible to independently observe the bulk through-plane variations in the Li-concentration during battery operation (*56*) with time resolution of order 20 min. At moderate spatial resolution of 50 μm, one can perform tomography on cylindrical cells as a function of the charge and discharge current (*55*).

To illustrate the utility of neutron imaging, a planar battery cell using highly oriented pyrolitic graphite (HOPG, dimension: 5 mm x 10 mm x 1 mm.) as the intercalating electrode and a piece of ^{6}Li metal as counter electrode was assembled. The two electrodes are separated laterally to avoid the overlap in neutron projection, and are in contact with 10 μm Ni foils on the opposing sides and connected to an external circuit. Neutron imaging was performed at the NIST neutron imaging facility, located on BT2 at the NIST Center for Neutron Research. In order to optimize the spatial resolution and measurement of the change in ^{6}Li concentration, the beam was set to have a collimation ratio of L/D = 600, which corresponds to a fluence rate of about $\Phi = 5 \times 10^{6}$ cm^{-2} s^{-1}. The CCD-lens system was configured to yield a field of view of about 4.5 cm × 4.5 cm with a spatial resolution of about 50 μm. Lithiation of HOPG at an electric current of -400 nA was captured using a time sequence picture framing of every 25 seconds over 20 hours.

The neutron image of the HOPG/^{6}Li cell is shown in Figure 11 (a). The attenuation of the neutron beam is the largest in regions of the highest ^{6}Li concentration; ^{6}Li appears dark and the pristine HOPG appears light. The images of HOPG upon lithiation for 5.9 min [Figure 11(b)], 41.0 min (c), 76.1 min (d), 111.2 min (e), 181.4 min (f), and 239.9 min (g) show highly non-uniform Li distribution in the HOPG, where the false-colored brighter regions are more concentrated in ^{6}Li. From a relatively Li-free initial state, 4 hotspots start to develop near the edge and at the surface of HOPG. As time goes by, more Li enter through those hotspots rather than creating new hotspots.

In Polymers for Energy Storage and Delivery: Polyelectrolytes for Batteries and Fuel Cells; Page, K., et al.;
ACS Symposium Series; American Chemical Society: Washington, DC, 2012.

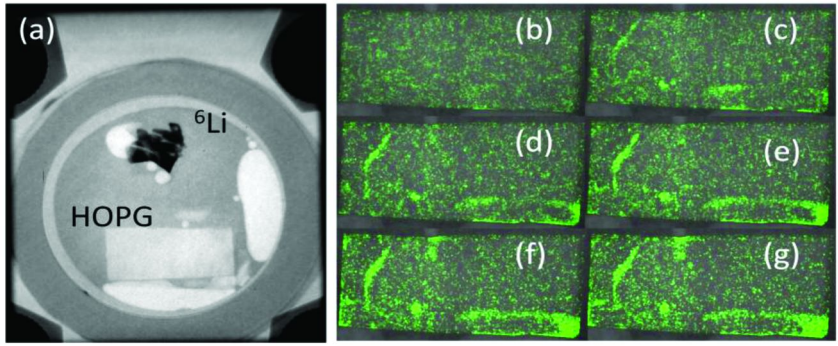

Figure 11. NI of HOPG lithiation (a) cell assembly, (b-g) time sequences of HOPG images

Considering that there are only 4 hotspots, each being of microscopic origin at the onset of lithiation, over the entire macroscopic HOPG crystal, we imagine that lithiation heterogeneity occurs over wide length scales, ranging from individual graphite particles in the order of 10 μm to the thickness of electrode layer to the dimension of battery cells. The activation and evolution of transport hotspots would pose new challenges in quantitative modeling of equivalent circuits and electrochemical performance of batteries. *In situ* NI can help construct more accurate circuit models for the design and optimization of the next generation secondary batteries.

Summary

The application of four *in situ* neutron measurement techniques for studying lithium ion batteries, neutron depth profiling (NDP), neutron reflectivity (NR), small angle neutron scattering (SANS), and neutron imaging (NI) are discussed in this chapter. In addition to introducing fundamentals and physical principles of each technique, their potential applications to studying battery systems are illustrated with specific examples. In each example, special battery cells were constructed and suitable charge/discharge rates were used to enable neutron measurements while maintaining the equivalent electrochemistry of battery operations. As those techniques together provide multi-scale measurements of the Li distribution and transport in active LIBs to yield valuable new insights in the performance and failure of battery systems, further development of neutron techniques is needed to meet the increasing demands in spatial, temporal and composition resolutions in battery research. Complementing other *in situ* and *ex situ* measurement techniques, neutron diagnoses could play a critical role in the design and development of future batteries with greater safety and reliability, higher energy and power density, and lower cost.

In Polymers for Energy Storage and Delivery: Polyelectrolytes for Batteries and Fuel Cells; Page, K., et al.;
ACS Symposium Series; American Chemical Society: Washington, DC, 2012.

Acknowledgments

HW acknowledges the financial support of General Motors Companry and University of Maryland through NIST-ARRA program.

References

1. Whittingham, M. S. *Science* **1976**, *192*, 1126–1127.
2. Whittingham, M. S. *MRS Bull.* **2008**, *33*, 411–419.
3. Tarascon, J. M.; Armand, M. *Nature* **2008**, *451*, 652–657.
4. Goodenough, J. B.; Kim, Y. *Chem. Mater* **2010**, *22*, 587–603.
5. Huang, J. Y.; et al. *Science* **2010**, *330*, 1515–1520.
6. Liu, X. H.; et al. *Nano Lett.* **2011**, *11*, 2251–2258.
7. Balke, N.; et al. *Nat. Nanotechnol.* **2010**, *5*, 749–754.
8. Kalinin, S. V.; et al. *ACS Nano* **2011**, *5*, 5683–5691.
9. Bhattacharyya, R.; et al. *Nat. Mater.* **2010**, *9*, 504–510.
10. Baris, K.; et al. *J. Am. Chem. Soc.* **2011**, *133*, 503–512.
11. Russenbeek, J.; et al. *J. Power Sources* **2011**, *196*, 2332–2339.
12. Shin, H. C.; et al. *Electrochim. Acta* **2011**, *56*, 1182–1189.
13. Sharma, N.; et al. *J. Power Sources* **2010**, *195*, 8258–8266.
14. Sharma, N.; et al. *Solid State Ionics* **2011**, *199-200*, 37–43.
15. Sharma, N.; et al. *J. Phys. Chem. C* **2011**, *115*, 21473–21480.
16. Rodriguez, M. A.; et al. *Electrochem Solid-State Lett.* **2004**, *7*, A8–10.
17. Rosciano, F.; Holzapfel, M.; Scheifele, W.; Novak, P. *J. Appl. Crystallogr.* **2008**, *41*, 690–694.
18. Colin, J. F.; Godbole, V.; Novák, P. *Electrochem. Comm.* **2010**, *12*, 804–807.
19. Du, G.; et al. *Adv. Funct. Mater.* **2011**, *21*, 3990–3997.
20. Bergstom, O.; Andersson, A. M.; Edstrom, K.; Gustafsson, T. *J. Appl. Cryst.* **1998**, *31*, 823–825.
21. Downing, R. G.; Lamaze, G. P.; Langland, J. K.; Hwang, S. T. *NIST J. Research* **1993**, *98*, 109.
22. Biersack, J. P.; Fink, D. *Nucl. Instr. Meth.* **1973**, *108*, 397–399.
23. Lamaze, G. P.; et al. *J. Power Sources* **2003**, *680*, 119–121.
24. Whitney, S. M.; Biegalski, S. R. F.; Downing, R. G. *J. Radioanal. Nucl. Chem.* **2009**, *282*, 173–176.
25. Whitney, S. M.; Biegalski, S. R.; Huang, Y. H.; Goodenough, J. B. *J. Electrochem. Soc.* **2009**, *156*, A886–A890.
26. Danilov, D.; Niessen, R. A. H.; Notten, P. H. L. *J. Electrochem. Soc.* **2011**, *158*, A215–A222.
27. Shrikant, C.; Nagpure, R.; Downing, R. G.; Bhushan, B.; Babu, S. S.; Cao, L. *Electrochimica Acta* **2011**, *56*, 4735–4743.
28. Oudenhoven, J. F. M.; Labohm, F.; Mulder, M.; Niessen, R. A. H.; Mulder, F. M.; Notten, P. H. L. *Advanced Materials* **2011**, *23*, 4103–4106.
29. Ziegler, J. F.; Ziegler, M. D.; Biersack, J. P. *Nucl Instrum Methods Phys Res B* **2010**, *268*, 1818–1823.
30. Owejan, J. E.; Owejan, J. P.; DeCaluwe S. C.; Dura J. A. (to be published)

In Polymers for Energy Storage and Delivery: Polyelectrolytes for Batteries and Fuel Cells; Page, K., et al.; ACS Symposium Series; American Chemical Society: Washington, DC, 2012.

31. Krueger, S.; Meuse, C. W.; Majkrzak, C. F.; Dura, J. A.; Berk, N. F.; Tarek, M.; Plant, A. L. *Langmuir* **2001**, *17*, 511.
32. Seah, M. P.; et al. *Surf. Interface Anal.* **2004**, *36*, 1269–1303.
33. Seah, M. P.; et al. *Surf. Interface Anal.* **2009**, *41*, 430–439.
34. Kent, M. S.; et al. *Macromolecules* **1992**, *25*, 6240–6247.
35. Majkrzak, C. F.; et al. In *Neutron Scattering in Biology: Techniques and Applications*; Fitter, J., Gutberlet, T., Katsaras, J., Eds.; Springer: 2006; pp 225–263.
36. Wacklin, H. P. *Curr. Opin. Colloid Interface Sci.* **2010**, *15*, 445–454.
37. Dura, J. A.; et al. *J. Appl. Phys.* **2011**, *109*, 093501.
38. Rehm, Ch.; Maletta, H.; Fieber-Erdmann, M.; Holub-Krappe, E.; Klose, F. *Phys. Rev. B* **2002**, *65*, 113404.
39. Russell, T. P. *Mater. Sci. Rep.* **1990**, *5*, 171–271.
40. Dura, J. A.; Murthi, V. S.; Hartman, M.; Satija, S. K.; Majkrzak, C. F. *Macromolecules* **2009**, *42*, 4769–4774.
41. Fitzsimmons M. R.; Majkrzak, C. F. In *Modern Techniques for Characterizing Magnetic Materials*; Zhu, Y., Ed.; Kluwer Acedemic Publishers: Boston, 2005.
42. Hjorvarsson, B.; et al. *Phys. Rev. Lett.* **1997**, *79*, 901.
43. Majkrzak, C. F. *Physica B* **1995**, *213*, 904.
44. Dura, J. A.; Pierce, D. J.; et al. *Rev. Sci. Instrum.* **2006**, *77*, 074301.
45. Majkrzak, C. F.; et al. *Physica B* **1998**, *248*, 338–342.
46. Kienzle, P. A.; O'Donovan, K. V.; Ankner, J. F.; Berk, N. F.; Majkrzak, C. F. http://www.ncnr.nist.gov/reflpak, 2000−2006.
47. Parratt, L. G. *Phys. Rev.* **1954**, *95*, 359.
48. Rolison, D. R.; Nazar, L. F. *MRS Bull.* **2011**, *36*, 486.
49. Details of SANS data analysis could be found in NIST wetsite: http://www.ncnr.nist.gov/programs/sans/data/red_anal.html.
50. Markervich, E.; Salitra, G.; Levi, M. D.; Aurbach, D. *J. Power Sources* **2005**, *146*, 146–150.
51. Aurbach, D.; Koltypin, M.; Teller, H. *Langmuir* **2002**, *18*, 9000–9009.
52. Rhodes, K.; Kirkham, M.; Meisner, R.; Parish, C. M.; Dudney, N.; Daniel, C. *Rev. Sci. Instrum.* **2011**, *82*, 075107.
53. Shearing, P. R.; Howard, L. E.; Jørgensen, P. S.; Brandon, N. P.; Harris, S. J. *Electrochem. Commun.* **2010**, *12*, 374–377.
54. Goers, D.; et al. *J. Power Sources* **2004**, *130*, 221–226.
55. Riley, G. V.; Hussey, D. S.; Jacobson, D. L. *ECS Trans.* **2009**, *25*, 75–83.
56. Siegel, J. B.; et al. *J. Electrochem. Soc.* **2011**, *158*, A523–A529.
57. Nikolay, K.; et al. *Mater. Today* **2011**, *14*, 248–256.
58. Hussey, D. S.; Jacobson, D. L.; Coakley, K. J.; Vecchia, D. F.; Arif, M. *ASME J. Fuel Cell Sci. Technol.* **2010**, *7*, 021024.